Excitons and exciton-phonon coupling in metallic single-walled carbon nanotubes: Resonance Raman spectroscopy

Stephen K. Doorn,[1,*] Paulo T. Araujo,[2] Kenji Hata,[3] and Ado Jorio[2,4]
[1]*Chemistry Division, Los Alamos National Laboratory, Los Alamos, New Mexico 87545, USA*
[2]*Departamento de Física, Universidade Federal de Minas Gerais, Belo Horizonte, MG, 30123-970 Brazil*
[3]*Research Center for Advanced Carbon Materials, AIST, Tsukuba, 305-8565, Japan*
[4]*Divisão de Metrologia de Materiais, Instituto Nacional de Metrologia, Normalização e Qualidade Industrial (INMETRO), Duque de Caxias, RJ, 25250-020, Brazil*
(Received 28 February 2008; revised manuscript received 9 June 2008; published 8 October 2008)

The first four transitions (upper and lower branches of E_{11}^M and E_{22}^M) for a broad diameter range (0.7–4 nm) of metallic single-walled carbon nanotubes are studied in the 1.26–2.71 eV energy range using resonance Raman spectroscopy of their radial breathing modes (RBMs). A scaling-law analysis of transition energies from 77 spectral features suggests that the transitions are excitonic in nature and that relative scaling of electron self-energies and exciton binding energies in metallic nanotubes closely matches that found in semiconductors. The previously elusive upper-branch signatures are observed at large diameters ($>$1.3 nm) for several chiralities for both E_{11}^M and E_{22}^M excitation. These results are discussed as a consequence of the nodal behavior of exciton-phonon coupling. Additionally, while theoretical calculations for the (n,m)-dependent matrix elements predict that the RBM intensity should decrease with increasing diameter, the opposite behavior is observed experimentally. We show that this is a consequence of an increase in the resonance Raman broadening factor Γ as diameter decreases.

DOI: 10.1103/PhysRevB.78.165408 PACS number(s): 78.67.Ch, 73.22.−f, 78.30.−j

I. INTRODUCTION

The one-dimensional (1D) nature of single-walled carbon nanotubes (SWNTs) results in unique materials and electronic and optical properties of particular interest for future nanoscale electronic and photonic applications.[1,2] Given their high conductivities, metallic SWNTs are envisioned for uses ranging from high-efficiency electronic interconnects to transparent conductive thin films.[3] Suitability for such applications is ultimately determined by the underlying electronic structure of the nanotubes and its interaction behavior with the phonon density of states through electron-phonon coupling and its impact on transport characteristics.[4] Of recent interest are predictions for the occurrence of strongly bound excitons that suggest nanotubes as model systems for probing novel exciton behavior in 1D metals.[5]

Optical studies of semiconducting SWNTs have been critical for developing an understanding of their chirality-dependent properties in terms of excitonic behavior.[6] By comparison, only limited spectroscopic data are available on metallic nanotubes. Of the two branches created by trigonal warping splitting of the metallic optical transitions (E_{11L}^M and E_{11H}^M for lower and higher branches, respectively),[7,8] early single-nanotube Raman studies[9] have yielded some results for E_{11L}^M, which has been complemented by more recent, but limited, probing of higher-order transitions with Rayleigh scattering techniques.[10] While single tube studies have provided important data, in many respects, ensemble measurements remain important for large-scale screening of properties. Such measurements [via resonance Raman spectroscopy of the SWNT radial breathing modes (RBMs)] on small-diameter (0.6–1.3 nm) metallics exist, but are limited to E_{11L}^M, while the upper-branch signatures remain elusive.[11–13] The inability to detect the upper branch in Raman measurements has been related to weak exciton-phonon coupling.[13,14] However, this coupling behavior can be complex[15–17] and needs to be probed further experimentally. Furthermore, the experimental demonstration of even the existence of excitons in 1D metals is only now being addressed.[18]

In this paper we present a determination of 77 metallic SWNT transition energies (in the 1.26–2.71 eV energy range) determined from resonance Raman spectroscopy of the RBM. Transitions measured include upper and lower branches as well as energies for the E_{22}^M level. The data are used to evaluate the success of recent extended tight-binding (ETB) calculations on these states. Scaling-law behavior[19,20] of the energies matches that found for excitonic transitions in semiconducting SWNTs, strongly suggesting the existence of excitons in these 1D metallic systems. Surprising diameter-dependent intensity behavior is also observed. In particular, we now observe the upper-branch features but only for the larger-diameter ($>$1.3 nm) nanotubes. Additionally, upper-branch intensities are found to be significant, while overall the RBM intensities tend to increase with diameter, in contrast with current theoretical models.[14–17] These observations are consistent with expectations based on the occurrence of nodal behavior in the exciton-phonon coupling elements[16,21] and with our observations that the resonance Raman broadening factor Γ increases significantly as nanotube diameter decreases.

II. EXPERIMENT

We collect resonance Raman spectral data in the RBM region from an intact as-produced nanotube vertical array. The carbon nanotube sample was produced via the water-assisted CVD "supergrowth" method.[22–25] This method produces millimeter-long isolated SWNTs of high purity with

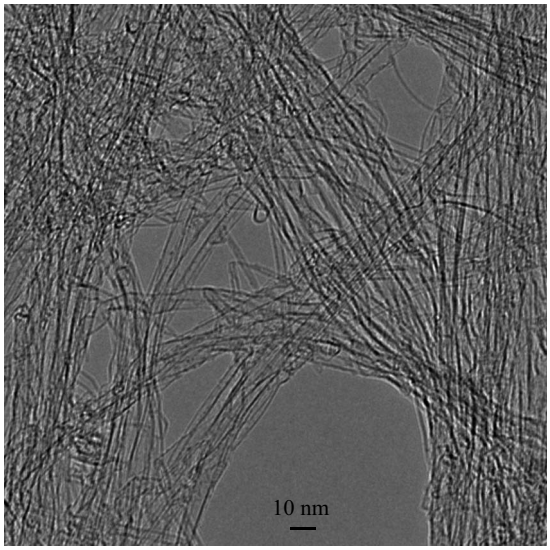

FIG. 1. Representative TEM image of nanotubes isolated from a supergrowth nanotube array.

diameters ranging from 0.7 to 4 nm. A TEM image of a representative sample of the supergrowth nanotubes is shown in Fig. 1 and is obtained from nanotubes dispersed onto a TEM grid. We find the SWNT content to be >99.9% with double-walled and few-walled nanotubes only rarely being found. Typical Raman D/G mode intensity ratios are found to be 0.1–0.2.

Raman measurements are made in a backscattering geometry using two triple monochromator Raman spectrometers (Dilor XY and SPEX for experiments in the visible and near-infrared ranges, respectively) with charge coupled device detection. An Ar-Kr laser and two tunable (dye and Ti:Sapphire) lasers are used for sample excitation at 125 different excitation energies (from 1.26 to 2.71 eV). Laser power densities are maintained constant and below heating effect thresholds (1 mW focused with an 80× objective in the visible range and 25 mW focused with a 10 cm focal length lens in the near-infrared range). Raw spectral intensities are corrected for instrument response and v^4 dependence. We fit experimental RBM excitation profile intensities (I_{RBM}) as a function of laser excitation energy (E_{laser}) to Eq. (1) to extract values for intensity maximum, transition energy (E_{ii}), and broadening factor (Γ);

$$I_{\mathrm{RBM}} = C\left|\frac{M}{\left(E_{ii} - E_{\mathrm{laser}} - \frac{i\Gamma}{2}\right)\left(E_{ii} - E_{\mathrm{laser}} - \hbar\omega_{\mathrm{RBM}} - \frac{i\Gamma}{2}\right)}\right|^2. \quad (1)$$

In Eq. (1), the parameter M represents the exciton-photon and exciton-phonon coupling matrix elements and C includes the effects of experimental acquisition parameters. During the modeling process, M, E_{ii}, and Γ are fit as adjustable parameters, while ω_{RBM} is fixed at the experimentally determined RBM frequency.

III. RESULTS AND DISCUSSION

A. Transition energies for metallic nanotubes

Figure 2 presents a summary of the collected Raman data. In addition to semiconducting features through the E_{66}^S transitions, we also observe (as highlighted) a broad range of E_{11}^M and E_{22}^M features. Of particular note is that, for the larger-diameter metallic species (>1.3 nm, corresponding to inverse Raman shift values of $>5.7\times10^{-3}$ cm in Fig. 2), we observe a number of the previously elusive upper-branch features in both E_{11}^M and E_{22}^M. While the TEM image in Fig. 1 shows a number of kink and other defect types in the supergrowth sample, the ability to observe the upper-branch features suggests that this is a high quality sample for enabling spectroscopic observations. Chirality assignments are made to spectral features by first deconvoluting each of the spectra into their individual Lorentzian components and pairing the resultant RBM frequencies (ω_{RBM}) with their respective excitation energy maxima. As in previously described approaches,[11,12,19,26] experimental plots of transition energy vs ω_{RBM} (or inverse diameter) reveal family patterns that allow the identification of $2n+m$=constant spectral groupings. Our assignments are facilitated by the comparison of such a plot to expected positions calculated within an ETB model[27,28] that accounts for curvature and many-body effects [Fig. 3(a)]. The one-to-one correspondence of the experimental and calculated features in Fig. 3(a) allows us to assign 77 RBM excitation features to their respective metallic (n,m) structures (see also, for supplemental information, Ref. 29).

For comparison to theory, it is important to note that all transition energies determined from this sample, for both semiconducting and metallic types, are found to be blue-shifted from energies previously found for other nanotube sample types.[30] This includes a ~40 meV upshift from values found for surfactant-suspended HiPco nanotubes and alcohol-assisted CVD samples. This finding suggests minimal environmental interactions for the nanotubes in this sample including a lack of intertube interactions from bundling, which is known to significantly redshift the observed transitions.[11,31] Further support for minimization of environmental and intertube interactions in the supergrowth sample is found in our observation of a global downshift in RBM frequencies relative to previously reported values. This is due primarily to a decrease in the van der Waals forces between the SWNTs in our sample and their environment as modeled and discussed more fully in Ref. 30. These results are also in agreement with high surface area measurements (80% of theoretical) on this sample type.[25]

The experimental points in Fig. 3(a) are in good agreement with their theoretical counterparts and are found to match well to the expected family patterns. We find that there is a systematic deviation of the theoretical values from the experimental points, with values being underestimated at larger diameters and overestimated at smaller diameter. The difference between the experimental and theoretical values as a function of inverse diameter [Fig. 3(b)] shows a strong linear dependence possibly arising from how diameter-dependent exciton screening is treated within the theory.

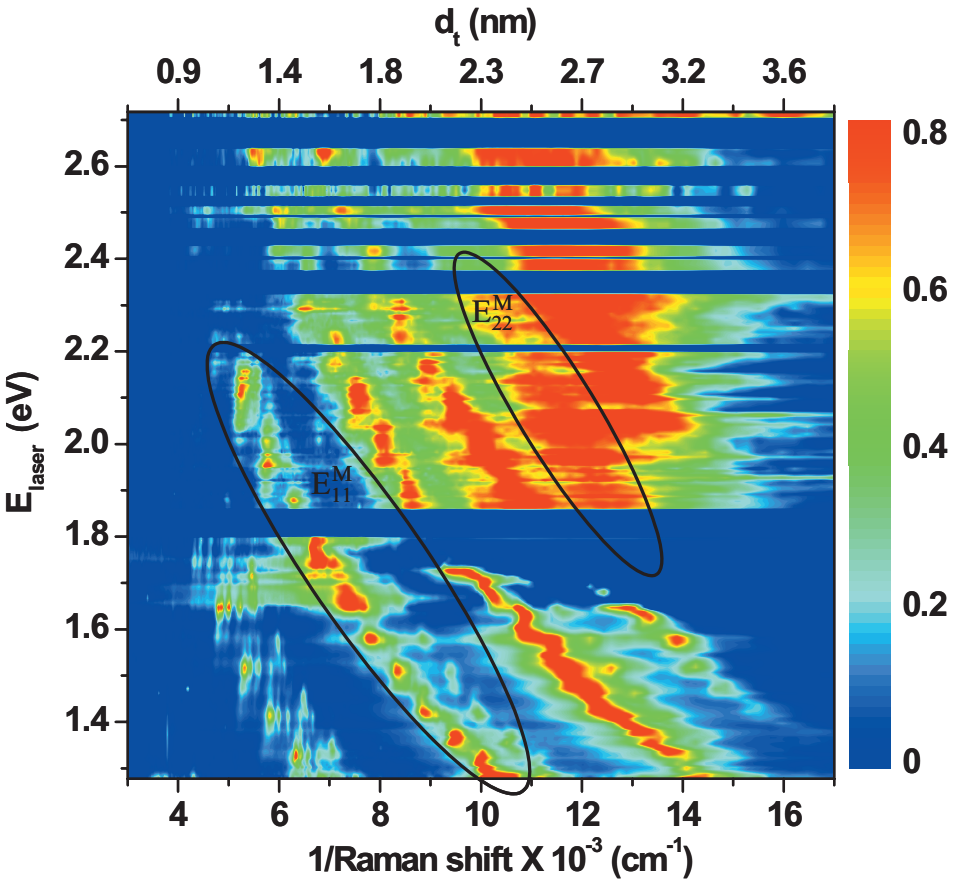

FIG. 2. (Color) Two-dimensional (2D) Raman excitation map showing the RBM intensity as a function of laser excitation energy and the inverse of the Stokes-Raman frequency (proportional to nanotube diameter). Each spectrum composing the plot has been normalized by the strongest peak for better clarity of the RBM resonances. The E_{11}^M and E_{22}^M features are highlighted. The upper axis is obtained considering $\omega_{\mathrm{RBM}}=227.0/d_t$ (Ref. 30).

For eight chiralities we are able to obtain sufficiently clear spectral features to allow the simultaneous extraction of energies for both the upper and lower branches (not simultaneously available for other metallic species for which the upper branches were observed; see, for supplemental information, Ref. 29) presenting the opportunity to directly evaluate the trigonal warping-induced splitting. In Fig. 3(c) we plot the difference between the available lower- and upper-branch energies and compare values to the ETB expectations. Differences between theory and experiment range from 4 to 60 meV. The splitting shows a linear dependence with $1/d_t$ that approaches zero in the large-diameter limit, in agreement with expectations.[7,8] Although only one point in Fig. 3(c) is from E_{22}^M, there is a clear break in splitting behavior as one goes to higher-order transitions. While further experimental data are necessary to explore this behavior, the increased splitting is expected as a result of the asymmetry of the trigonal warping effect in different directions within the Brillouin zone, which yields an increased dispersion along the K-Γ direction (compared to that in the K-M direction) as one moves further from the K point for higher-order transitions. The E_{22H}^M energy thus increases faster than E_{22L}^M and results in an increased splitting relative to that found for E_{11}^M.

B. Excitons in metallic nanotubes

We have found it useful to explore the energies of semiconducting nanotubes in terms of a scaling-law analysis that reveals trends in excitonic behavior.[19,32] We apply the same approach to the metallic transitions by plotting (Fig. 4) the observed transition energies (E_{expt}) [after removing their chiral-angle (θ) dependence by subtracting the term $(\beta_p \cos 3\theta)/d_t^2$, where β_p is −0.18(+0.29) and −0.60(+0.57) for $E_{11L}^M(E_{11H}^M)$ and $E_{22L}^M(E_{22H}^M)$, respectively] as a function of p/d_t (where $p=1$, 2, 3, 4, 5, and 6 for E_{11}^S, E_{22}^S, E_{11}^M, E_{33}^S, E_{44}^S, and E_{22}^M, respectively, and d_t is nanotube diameter) according to Eq. (2)

$$E_{\mathrm{expt}} - (\beta_p \cos 3\theta)/d_t^2 = a\frac{p}{d_t}\left(1 + b\log\frac{c}{p/d_t}\right). \qquad (2)$$

E_{11}^S and E_{22}^S for this sample fit this expression closely with $a=1.074$ eV nm, $b=0.467$, and $c=0.812$ nm^{-1} (as represented by the lower solid line in Fig. 4), while E_{33}^S and E_{44}^S are well fit by adding the value $0.0596p/d_t$ to this expression (as represented by the upper line in Fig. 4). Kane and Mele[20] showed that such a nonlinear scaling relation results from a renormalization of the Coulomb energy that arises from treating the close-range many-body interactions of 2D graphene as a noninteracting quasiparticle. For the 1D nanotube system, long-range interactions strongly increase this quasiparticle gap, but in semiconductors the observed effect is significantly reduced due to the exciton binding energy. Thus, while the diameter dependence of the transition energies is defined by the logarithmic scaling, their absolute energy position is ultimately determined by the difference between the electron self-energy and the exciton binding energy.

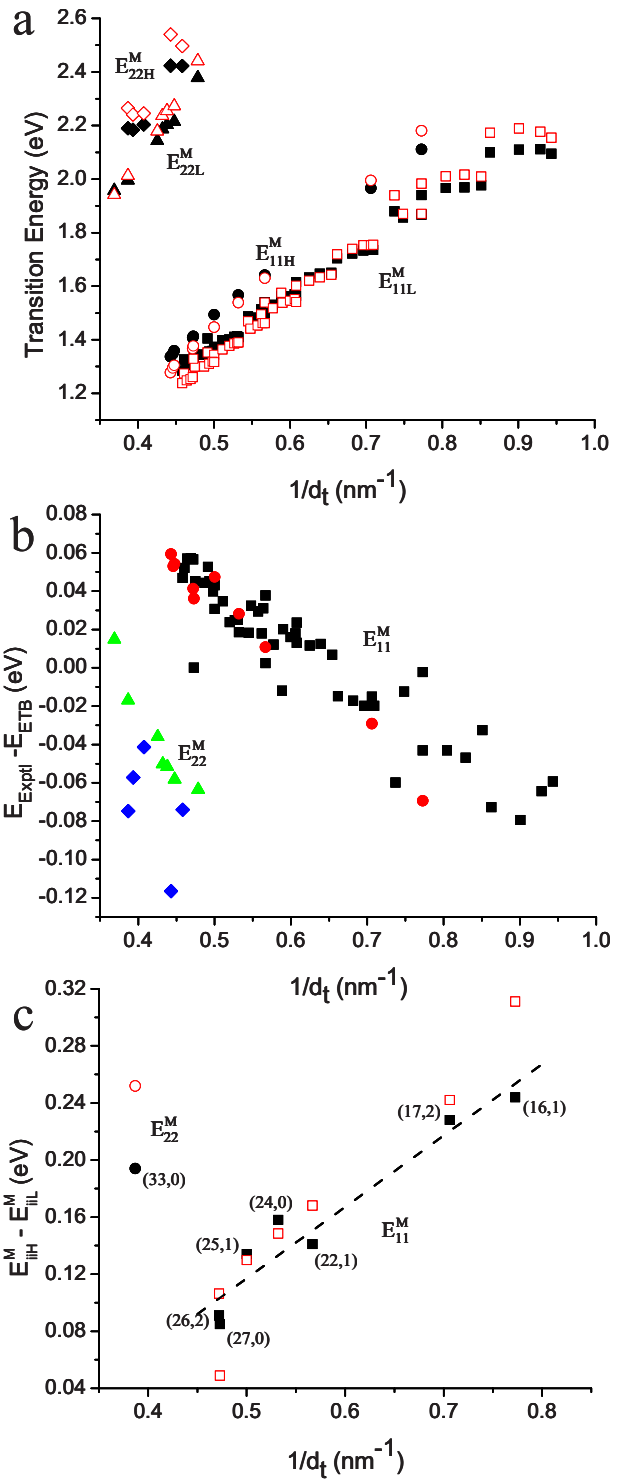

FIG. 3. (Color online) (a) A comparison of experimental (solid symbols) and ETB-determined (Ref. 28) (open symbols) metallic transition energies as a function of inverse nanotube diameter for E^M_{11L} (squares), E^M_{11H} (circles), E^M_{22L} (triangles), and E^M_{22H} (diamonds). (b) Difference in energy between experimental and ETB-determined results as a function of inverse nanotube diameter for E^M_{11L} (squares), E^M_{11H} (circles), E^M_{22L} (triangles), and E^M_{22H} (diamonds). (c) Energy splittings (E^M_{iiH}-E^M_{iiL}) for experimental (solid symbols) and ETB-determined (Ref. 28) (open symbols) transitions. Specific (n,m) species are identified. The dashed line is a linear fit to the E^M_{11} experimental data with $(E^M_{11H}$-$E^M_{11})=0.5/d_t-0.13$.

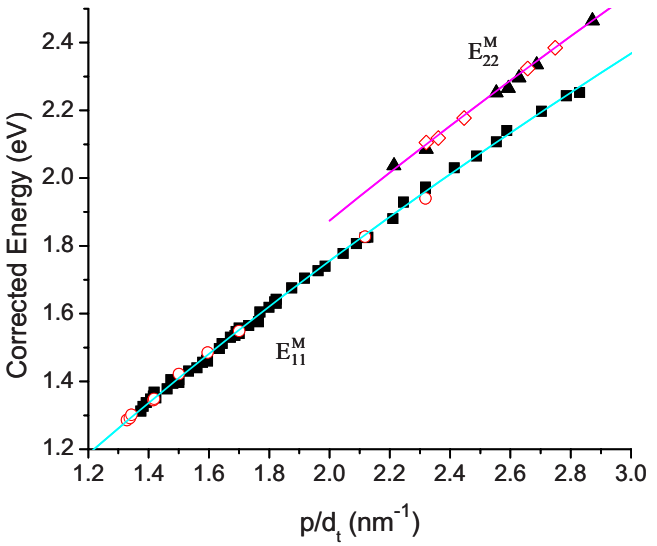

FIG. 4. (Color online) Chiral-angle-dependence-corrected E^M_{11} and E^M_{22} energies $[E_{\mathrm{expt}}-(\beta_p \cos 3\theta)/d_t^2]$ for lower (solid symbols) and upper (open symbols) branches as a function of p/d_t, where $p=3$ and 6, respectively. Scaling-law trend lines (Refs. 19 and 20) for E^S_{11} and E^S_{22} (lower line) and E^S_{33} and E^S_{44} (upper line) observed in our sample are shown for comparison.

As applied to the metallic SWNTs, the data for both upper and lower branches within E^M_{11} and E^M_{22} (see Fig. 4) closely match the semiconducting trendlines. The excellent representation of the trend in the metallic transition energies by the semiconductor logarithmic scaling law is indirect evidence that the metallic transitions are also excitonic in nature. If one first assumes no exciton, then it is possible that significant metallic screening reduces the E^M_{11} self-energies sufficiently to allow for a coincidental overlap with the E^S_{11} and E^S_{22} scaling line. A simultaneous overlap of E^M_{22} with the E^S_{33} and E^S_{44} scaling line, however, is unlikely in the absence of the exciton. Lack of the binding-energy stabilization for E^M_{22} would cause its scaling line to appear above the E^S_{33} and E^S_{44} line, which (as seen in Fig. 4) is not the case. Thus, the existence of excitons in these 1D metals is strongly suggested over the full diameter and energy ranges measured here. This is a somewhat surprising result in that the large screening expected in metallic systems will not support the formation of a bound exciton. While this is true in 2D and three-dimensional systems, it has been shown recently that this expectation breaks down in the 1D case.[5] While screening remains large, it is dramatically reduced in the 1D case relative to expectations for bulk metals and significant binding energy remains (on the order of 50 meV),[5] indicating the importance of excitons in 1D metals. It is interesting to note that similar exciton binding energies are found in bulk semiconductors.

The strong overlap of the metallic and semiconducting trend lines suggests that, despite the increased screening and reduced binding energy in metallics, the difference between the electron self-energy and exciton binding-energy contributions remains nearly the same as in their semiconducting counterparts. This similarity in behavior between the electronic types can be understood in terms of the influence the

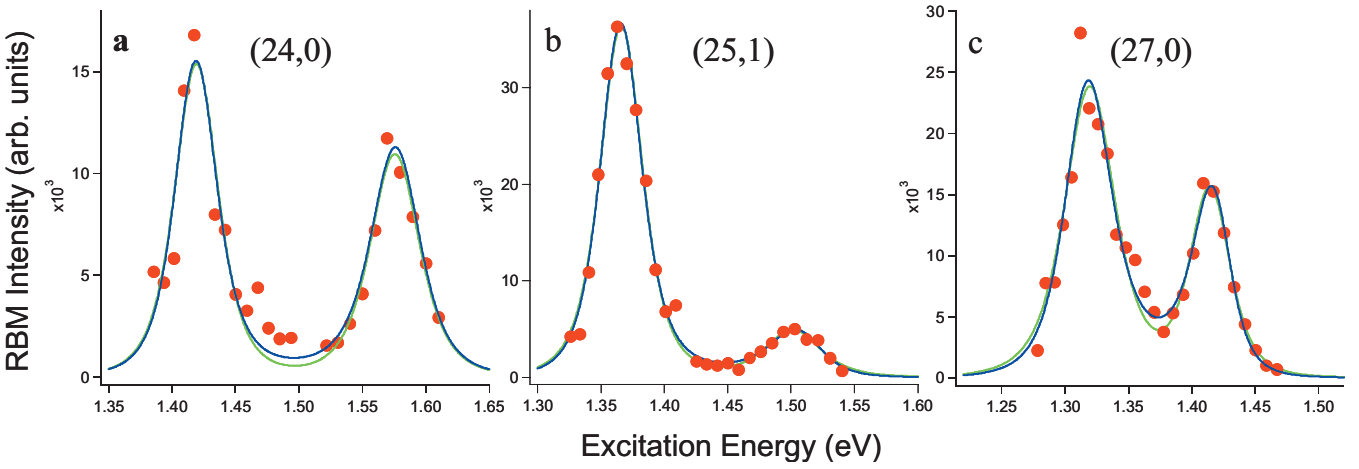

FIG. 5. (Color) Resonance Raman E_{11}^{M} excitation profiles for upper-/lower-branch pairs of three selected metallic species with (n,m) indices of (a) (24,0), (b) (25,1), and (c) (27,0). The solid lines are a fit to the data [using Eq. (1) with blue line including Raman interference effects and green line for no interference] to yield E_{ii} and Γ values of (a) no interference: E_{11L}^{M}=1.411 eV, E_{11H}^{M}=1.568 eV and Γ_L =56 meV, Γ_H=66 meV; with interference: E_{11L}^{M}=1.411 eV, E_{11H}^{M}=1.569 eV and Γ_L=55 meV,Γ_H=54 meV; (b) no interference: E_{11L}^{M} =1.359 eV, E_{11H}^{M}=1.494 eV and Γ_L=58 meV, Γ_H=79 meV; with interference: E_{11L}^{M}=1.358 eV, E_{11H}^{M}=1.501 eV and Γ_L=56 meV, Γ_H =71 meV; and (c) no interference: E_{11L}^{M}=1.312 eV, E_{11H}^{M}=1.408 eV and Γ_L=64 meV, Γ_H=53 meV; with interference: E_{11L}^{M}=1.310 eV, E_{11H}^{M}=1.412 eV and Γ_L=63 meV, Γ_H=48 meV.

electron and hole effective masses have on the Coulomb energy. The effective mass is directly related to the curvature of the energy dispersion within the Brillouin zone. E_{11}^{M} and E_{11}^{S} and E_{22}^{S} sample similar regions within the Brillouin zone, as do E_{22}^{M} and E_{33}^{S} and E_{44}^{S}. Thus, similar curvatures are experienced and the many-body effects should demonstrate related behaviors.

C. RBM intensity behavior

The electronic coupling to the RBM is a significant factor in determining the observed Raman intensities and is of particular interest for the metallic nanotubes since previous studies have shown no evidence for the occurrence of the upper-branch transitions via resonance Raman measurements.[11,12,19,26] In agreement with these previous results, we observe no upper-branch features at small diameters (<1.3 nm). However, beginning at diameters of about 1.3 nm and larger, the upper branches for zigzag and near-zigzag chiralities become evident (see Fig. 2). For all cases in which upper-branch features are observed, they are weaker than those of the corresponding lower branch [see for example Fig. 5(b)] but in some cases approach the lower-branch intensities [Figs. 5(a) and 5(c)].

Analogously to the semiconducting case, exciton-phonon coupling is expected to be stronger for transitions originating in the K-M valley and weaker for those from the K-Γ valley.[14] For all metallic SWNTs, the upper branch always originates in the K-Γ valley, giving rise to the expectation that the upper-branch transitions will be weak and difficult to observe.[14,26] Additionally, the coupling is expected to decrease in both branches as the diameter increases.[14–16] That we begin to see upper-branch features for the larger-diameter species seems counterintuitive. However, the valley origin rule provides only part of the picture.

Both analytical expressions[16] and numerical evaluations[21] of exciton-phonon coupling have demonstrated that transitions originating in the K-Γ valley exhibit nodal behavior that results in reduced coupling around the node. For appropriate chiralities, however, it is possible to push into a coupling regime beyond this node. Such "postnodal" behavior occurs at larger diameters.[16] It has been demonstrated that for certain semiconducting structures it is possible to obtain intensities from the K-Γ valley that approach those for transitions originating from the K-M valley.[16] Numerical results show that this behavior at larger diameters is a general property for both metallic and semiconducting species with one consequence of the nodal behavior being that, as the value of $(n$-$m)$ increases for a fixed diameter, the exciton-phonon coupling strength increases.[15] The largest values of $(n$-$m)$ can be obtained for near-zigzag chiralities and also for large-diameter nanotubes. As with semiconductors, values of $(n$-$m)$ exist at large diameter for which metallic upper- and lower-branch intensities can be closely matched.[15,16] These predictions are supported by the results shown in Fig. 5. The direct comparison of upper- and lower-branch intensities for the chiralities shown in Fig. 5 demonstrates that upper-branch intensities can indeed be quite significant and of similar strength as the lower-branch features. Additionally, consistent with all descriptions of exciton-phonon coupling in SWNTs, we observe the upper-branch features for structures with chiral angles of $<10°$ in nearly all cases.

One consequence of the upper-branch transition appearing in close proximity to that of the lower branch is the possibility of observing Raman interference effects.[21,33] We explore this possibility by fitting the experimental data of Fig. 5 in two different ways. The first includes interference by summing the contributions for the two transitions at the amplitude level [before squaring the polarizability in Eq. (1)]. The second assumes no interference and simply treats the intensity contributions from the two transitions as additive. We

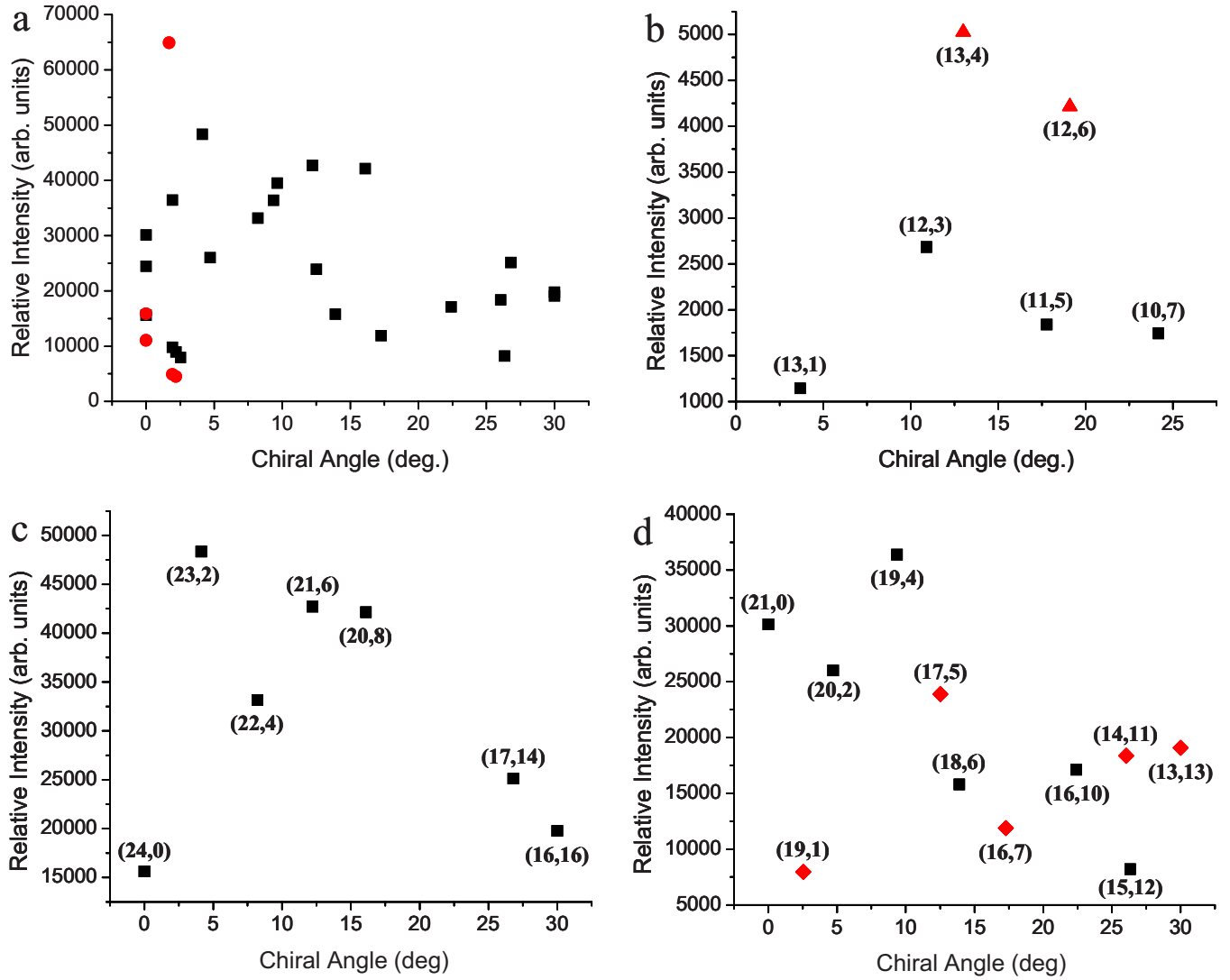

FIG. 6. (Color online) Plots of maximum RBM intensities (all with E_{11}^M excitation) as a function of chiral angle. (a) E_{11}^M lower-branch (squares) and upper-branch (circles) intensities (data from near-IR excitation only). RBM intensities for lower branches of selected families with $2n+m$=constant (b) $2n+m$=30 (triangles) and 27 (squares) (data from visible excitation only). (c) $2n+m$=48 (data from near-IR excitation only). (d) $2n+m$=42 (squares) and 39 (diamonds) (data from near-IR excitation only).

find only minor differences in the results [transition energy and Γ are affected by 1–7 meV; and 12 meV in the case of Γ (upper) for the (24,0) chirality] indicating that, for the observed energy splittings, interference effects are minimal. For structures with larger chiral angle, the splittings will be smaller, but we anticipate minimal interference effects in such cases due to the lack of intensity in the upper branch from minimization of the exciton-phonon coupling for these chiralities as discussed above.

The general range of intensity behavior of additional chiralities is shown in Figs. 6 and 7. We note that intensities for small-diameter (<1.3 nm) E_{11}^M features [Figs. 6(b) and 7(c)] and all E_{22}^M [Fig. 7(d)] features cannot be directly compared to those for the larger-diameter (>1.3 nm) E_{11}^M as the data were obtained from different instruments. Despite the scatter in the data, which may reflect some degree of nonuniformity in the populations of any given chirality as well as inhomogeneous spatial distributions within the sample, some trends appear. In Fig. 6(a), a general decrease in intensity is observed as chiral angle increases. This is more clearly seen in Figs. 6(b)–6(d) for which this behavior is highlighted for specific families of $2n+m$=constant. Within a given $2n+m$ family, intensity decreases as chiral angle increases, in agreement with theoretical expectations and previous observations on semiconducting nanotubes.[14–17]

Diameter-dependent trends are shown in Fig. 7. Figure 7(a) shows a general decrease in intensity as diameter decreases, with the behavior being more clearly seen for the specific chiralities shown in Figs. 7(b)–7(d). This trend is present despite any complicating chiral-angle dependences (as discussed above), with nanotubes of near-zero chiral angle [Fig. 7(b)] clearly showing the intensity decrease with diameter. This trend is surprising as it is the reverse of the general theoretical expectation that the exciton-phonon coupling contribution to the intensity will decrease as diameter increases.[14–17] We find that this trend can be understood by

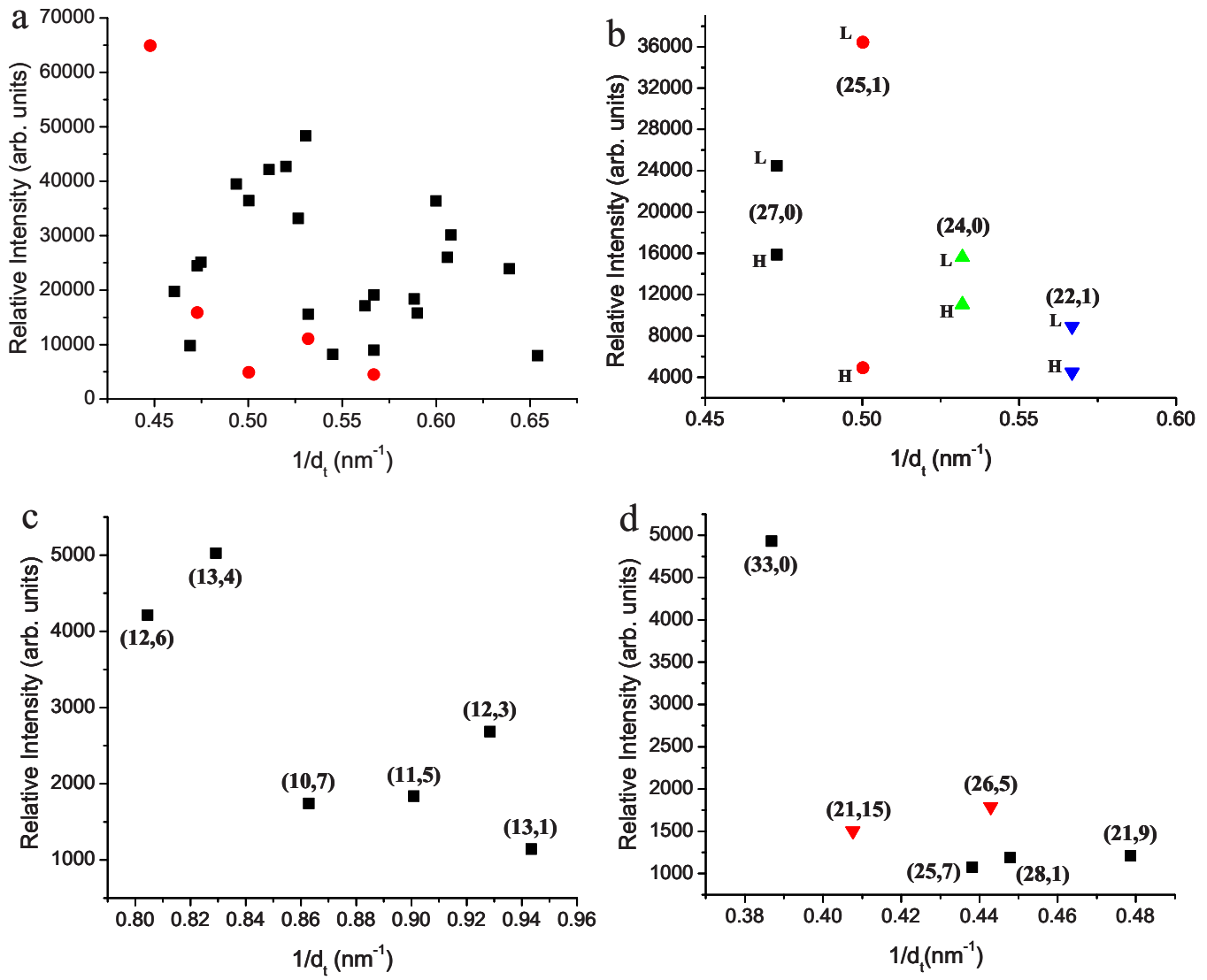

FIG. 7. (Color online) Plots of maximum RBM intensities as a function of inverse nanotube diameter $(1/d_t)$. (a) E_{11}^M lower-branch (squares) and upper-branch (circles) intensities (data from near-IR excitation only). (b) Comparison of lower- and upper-branch intensities of the four E_{11}^M transitions for which both excitation profiles are fully obtainable (data from near-IR excitation). (c) E_{11}^M intensities for small-diameter (<1.3 nm) nanotubes (data from visible excitation only). (d) E_{22}^M lower- (squares) and upper- (triangles) branch intensities (data from visible excitation only).

accounting for the diameter-dependent contribution of Γ in the Raman intensity expression [Eq. (1)].

Figure 8(a) shows a plot of Γ vs inverse diameter for the E_{11L}^M points shown in Figs. 6(a) and 7(a). Included in the plot are Γ values for E_{22}^S transitions observed in the same diameter and excitation energy region. A strong diameter dependence is observed with Γ increasing as diameter decreases. This is in excellent agreement with previously predicted behavior based on an evaluation of carrier lifetimes in metallic nanotubes as determined by electron-phonon interaction.[34] The theoretical results of Ref. 34 also suggest that plasmon excitation in metallic nanotubes will yield an additional contribution to Γ over what is expected in semiconducting chiralities, suggesting that Γ will generally be larger for metallics than for semiconductors. Our results support this conclusion. While Fig. 8(a) shows that semiconductor Γ values also increase as d_t decreases, the semiconductor behavior is displaced to lower values in comparison to metallic nanotubes of similar diameter. When one considers that it is the E_{22}^S values and not the smaller E_{11}^S Γ values[35,36] that we compare to the E_{11L}^M, the relative importance of the plasmon contribution to Γ is emphasized. This highlights an additional parallel found here in comparing metallic and semiconducting nanotube behaviors. In semiconductors, Γ has been found to increase significantly on going from E_{11}^S excitation to E_{22}^S and E_{33}^S.[32,35,36] This occurs for the metals as well, as seen in Fig. 8(b), in which E_{22L}^M Γ values are found to be a factor of 2 or more greater than for E_{11L}^M.

It is clear from Eq. (1) (and has been previously shown)[35] that such diameter-dependent and transition level effects on Γ will play as important a role in determining the RBM intensities as the chirality dependence of the exciton-phonon coupling matrix elements. The increase in Γ as diameter de-

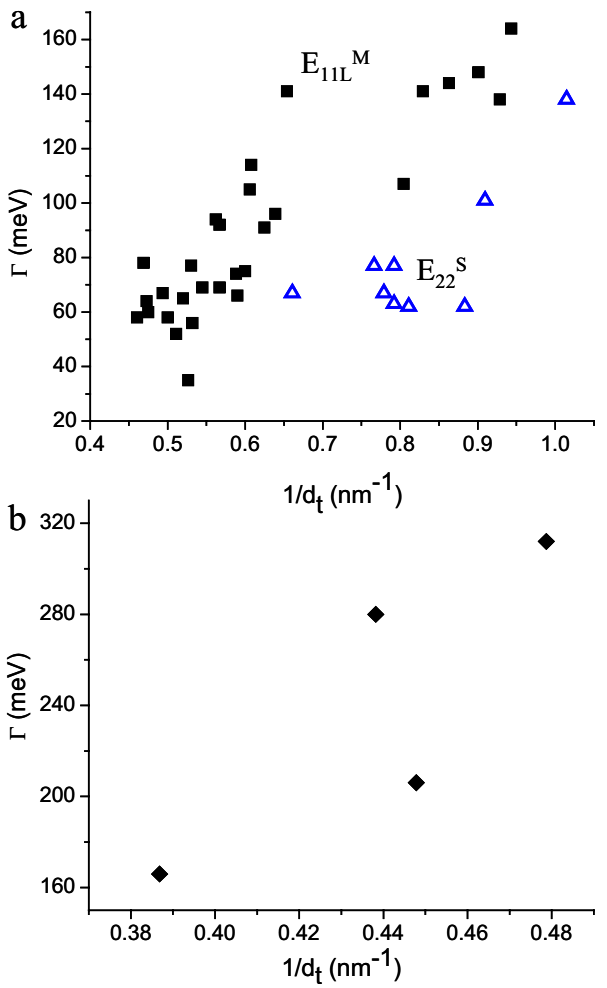

FIG. 8. (Color online) a) Plot of Γ as a function of inverse diameter obtained with E_{11L}^{M} excitation for metallic nanotubes (solid squares). Γ values for semiconductors obtained with E_{22}^{S} excitation (open triangles) are added for comparison. (b) Plot of Γ as a function of inverse diameter for E_{22L}^{M}.

creases will result in a reduction in Raman intensity and thus provides an explanation for the observed increase in intensity with diameter shown in Fig. 7. The diameter dependence of Γ overcomes the role played by exciton-phonon coupling in this case. It is also likely that this diameter dependence in Γ is in part responsible for the loss of upper-branch intensities at small diameters. In the diameter range for which the upper-branch features are not observed, Γ for the upper branch is predicted to be significantly larger than that of the lower branch.[34] The additional resultant loss in Raman intensity will multiply the effect from the expected decrease in the exciton-phonon coupling for the upper branch as discussed above. While for larger-diameter nanotubes we observe Γ values (Fig. 5 and Ref. 29) that are more similar between the upper and lower branches (also in agreement with theory),[34] the increased upper-branch broadening relative to that of the lower branch indicates that the postnodal behavior discussed above is still required to make the upper branches visible in this regime.

IV. CONCLUSIONS

In summary, the comprehensive analysis of 77 metallic transitions presented here demonstrates many parallels to the behaviors found in semiconducting SWNTs. The results of the scaling analysis underscore that Eq. (2) accurately describes the transition energies for both metallic and semiconducting SWNTs. This simple formula can be readily used by anyone to generate the E_{ii} of any SWNT of interest and is proving to be a powerful tool for extracting new insight into nanotube excitations.[19,32] Our result that excitonic behavior is supported in metallic SWNTs, despite the presence of significant screening, points toward their use as potential models for further probing of the unique properties of excitons in 1D metallic systems. Our results also demonstrate the generality of exciton-phonon coupling descriptions. Coupling of excitons to the RBMs follows the same principles previously observed for semiconductors. The metallic intensity behavior provides additional evidence for the occurrence of nodes in the exciton-phonon coupling matrix elements and different regions of exciton-phonon coupling strength. The observed Γ effects on intensity indicate a need for further theoretical studies aimed at understanding the interplay between Γ and the effects of phonon coupling to the electronic structure (including nodal behavior) in determining Raman intensities in these systems. Finally, we comment on the particular attributes of the supergrowth sample that have allowed the observation of the upper-branch spectral features. It is clear from our results that the correct diameter distribution must be present in the sample under study with the upper branches for nanotubes >1.3 nm in diameter being the most easily observed. Furthermore, our results also point to the importance of minimizing intertube interactions. It is likely, for example, that the upper branches may also be observed in solution-phase surfactant-suspended samples through the improved dispersions and narrower spectral linewidths found with the use of bile salts.[37]

ACKNOWLEDGMENTS

We thank Kentaro Sato and Riichiro Saito for providing the ETB data from Ref. 28 and Andy Shreve for valuable discussions. S.K.D. acknowledges support from the LANL LDRD program. P.T.A. acknowledges CNPq for financial support. A.J. acknowledges financial support under Universal Grants (CNPq and Fapemig) and by Rede Nacional de Pesquisa em Nanotubos de Carbono (MCT and CNPq). Sample growth was supported by the New Energy and Industrial Technology Development Organization (NEDO) Nano-Carbon Technology project.

*Author to whom correspondence should be addressed; skdoorn@lanl.gov

[1] A. Jorio, M. S. Dresselhaus, and G. Dresselhaus, *Carbon Nanotubes: Advanced Topics in the Synthesis, Structure, Properties, and Applications*, Springer Series in Topics in Applied Physics Vol. 111 (Springer-Verlag, Berlin, 2007).

[2] P. Avouris, Z. Chen, and V. Perebeinos, Nat. Nanotechnol. **2**, 605 (2007).

[3] Z. Wu, Z. Chen, Z. Du, J. M. Logan, J. Sippel, M. Nikolou, K. Kamaras, J. R. Reynolds, D. B. Tanner, A. F. Hebard, and A. G. Rinzler, Science **305**, 1273 (2004).

[4] Z. Yao, C. L. Kane, and C. Dekker, Phys. Rev. Lett. **84**, 2941 (2000).

[5] J. Deslippe, C. D. Spataru, D. Prendergast, and S. G. Louie, Nano Lett. **7**, 1626 (2007).

[6] M. S. Dresselhaus, G. Dresselhaus, R. Saito, and A. Jorio, Annu. Rev. Phys. Chem. **58**, 719 (2007).

[7] R. Saito, G. Dresselhaus, and M. S. Dresselhaus, Phys. Rev. B **61**, 2981 (2000).

[8] S. Reich and C. Thomsen, Phys. Rev. B **62**, 4273 (2000).

[9] A. Jorio, R. Saito, J. H. Hafner, C. M. Lieber, M. Hunter, T. McClure, G. Dresselhaus, and M. S. Dresselhaus, Phys. Rev. Lett. **86**, 1118 (2001).

[10] M. Y. Sfeir, T. Beetz, F. Wang, L. Huang, X. M. H. Huang, M. Huang, J. Hone, S. O'Brien, J. A. Misewich, T. F. Heinz, L. Wu, Y. Zhu, and L. E. Brus, Science **312**, 554 (2006).

[11] C. Fantini, A. Jorio, M. Souza, M. S. Strano, M. S. Dresselhaus, and M. A. Pimenta, Phys. Rev. Lett. **93**, 147406 (2004).

[12] H. Telg, J. Maultzsch, S. Reich, F. Hennrich, and C. Thomsen, Phys. Rev. Lett. **93**, 177401 (2004).

[13] H. Son, A. Reina, Ge. G. Samsonidze, R. Saito, A. Jorio, M. S. Dresselhaus, and J. Kong, Phys. Rev. B **74**, 073406 (2006).

[14] M. Machón, S. Reich, H. Telg, J. Maultzsch, P. Ordejon, and C. Thomsen, Phys. Rev. B **71**, 035416 (2005).

[15] J. Jiang, R. Saito, Ge. G. Samsonidze, S. G. Chou, A. Jorio, G. Dresselhaus, and M. S. Dresselhaus, Phys. Rev. B **72**, 235408 (2005).

[16] S. V. Goupalov, B. C. Satishkumar, and S. K. Doorn, Phys. Rev. B **73**, 115401 (2006).

[17] J. Jiang, R. Saito, K. Sato, and J. S. Park, Ge. G. Samsonidze, A. Jorio, G. Dresselhaus, and M. S. Dresselhaus, Phys. Rev. B **75**, 035405 (2007).

[18] F. Wang, D. J. Cho, B. Kessler, J. Deslippe, P. J. Schuck, S. G. Louie, A. Zettl, T. F. Heinz, and Y. R. Shen, Phys. Rev. Lett. **99**, 227401 (2007).

[19] P. T. Araujo, S. K. Doorn, S. Kilina, S. Tretiak, E. Einarsson, S. Maruyama, H. Chacham, M. A. Pimenta, and A. Jorio, Phys. Rev. Lett. **98**, 067401 (2007).

[20] C. L. Kane and E. J. Mele, Phys. Rev. Lett. **93**, 197402 (2004).

[21] J. Jiang, R. Saito, A. Gruneis, S. G. Chou, Ge. G. Samsonidze, A. Jorio, G. Dresselhaus, and M. S. Dresselhaus, Phys. Rev. B **71**, 205420 (2005).

[22] K. Hata, D. N. Futaba, K. Mizuno, T. Namai, M. Yumura, and S. Iijima, Science **306**, 1362 (2004).

[23] D. N. Futaba, K. Hata, T. Yamada, K. Mizuno, M. Yumura, and S. Iijima, Phys. Rev. Lett. **95**, 056104 (2005).

[24] D. N. Futaba, K. Hata, T. Namai, T. Yamada, K. Mizuno, Y. Hayamizu, M. Yumura, and S. Iijima, J. Phys. Chem. B **110**, 8035 (2006).

[25] D. N. Futaba, K. Hata, T. Yamada, T. Hiraoka, Y. Hayamizu, Y. Kakudate, O. Tanaike, H. Hatori, M. Yumura, and S. Iijima, Nature Mater. **5**, 987 (2006).

[26] J. Maultzsch, H. Telg, S. Reich, and C. Thomsen, Phys. Rev. B **72**, 205438 (2005).

[27] V. N. Popov and L. Henrard, Phys. Rev. B **70**, 115407 (2004).

[28] K. Sato, R. Saito, J. Jiang, G. Dresselhaus, and M. S. Dresselhaus, Phys. Rev. B **76**, 195446 (2007).

[29] See EPAPS Document No. E-PRBMDO-78-006840 for a tabulation of the observed metallic nanotube RBM frequencies, transition energies, Γ values, and (n,m) assignments. For more information on EPAPS, see http://www.aip.org/pubservs/epaps.html.

[30] P. T. Araujo, I. O. Maciel, P. B. C. Pesce, M. A. Pimenta, S. K. Doorn, H. Qian, A. Hartschuh, M. Steiner, L. Grigorian, K. Hata, and A. Jorio, Phys. Rev. B **77**, 241403(R) (2008).

[31] M. J. O'Connell, S. Sivaram, and S. K. Doorn, Phys. Rev. B **69**, 235415 (2004).

[32] E. H. Haroz, S. M. Bachilo, R. B. Weisman, and S. K. Doorn, Phys. Rev. B **77**, 125405 (2008).

[33] G. Bussi, J. Menendez, J. Ren, M. Canonico, and E. Molinari, Phys. Rev. B **71**, 041404(R) (2005).

[34] J. S. Park, Y. Oyama, R. Saito, W. Izumida, J. Jiang, K. Sato, C. Fantini, A. Jorio, G. Dresselhaus, and M. S. Dresselhaus, Phys. Rev. B **74**, 165414 (2006).

[35] B. C. Satishkumar, S. V. Goupalov, E. H. Haroz, and S. K. Doorn, Phys. Rev. B **74**, 155409 (2006).

[36] H. Telg, J. Maultzsch, S. Reich, and C. Thomsen, Phys. Status Solidi B **244**, 4006 (2007).

[37] W. Wenseleers, I. I. Vlasov, E. Goovaerts, E. D. Obraztsova, A. S. Lobach, and A. Bouwen, Adv. Funct. Mater. **14**, 1105 (2004).